PCCP

ROYAL SOCIETY OF CHEMISTRY

PAPER

View Article Online
View Journal | View Issue

Cite this: *Phys. Chem. Chem. Phys.*, 2021, **23**, 23544

Toward Å–fs–meV resolution in electron microscopy: systematic simulation of the temporal spread of single-electron packets

Wyatt A. Curtis and David J. Flannigan *

Received 31st July 2021,
Accepted 9th October 2021

DOI: 10.1039/d1cp03518e

rsc.li/pccp

Though efforts to improve the temporal resolution of transmission electron microscopes (TEMs) have waxed and waned for decades, with relatively recent advances routinely reaching sub-picosecond scales, fundamental and practical challenges have hindered the advance of combined Å–fs–meV resolutions, particularly for core-loss spectroscopy and real-space imaging. This is due in no small part to the complexity of the approach required to access timescales upon which electrons, atoms, molecules, and materials first begin to respond and transform – attoseconds to picoseconds. Here we present part of a larger effort devoted to systematically mapping the instrument parameter space of a TEM modified to reach ultrafast timescales. With General Particle Tracer, we studied the statistical temporal distributions of single-electron packets as a function of various fs pulsed-laser parameters and electron-gun configurations and fields for the exact architecture and dimensions of a Thermo Fisher Tecnai Femto ultrafast electron microscope. We focused on easily-adjustable parameters, such as laser pulse duration, laser spot size, photon energy, Wehnelt aperture diameter, and photocathode size. In addition to establishing trends and dispersion behaviors, we identify regimes within which packet duration can be 100s of fs and approach the 300 fs laser limit employed here. Overall, the results provide a detailed picture of the temporal behavior of single-electron packets in the Tecnai Femto gun region, forming the initial contribution of a larger effort.

Introduction

Four-dimensional ultrafast electron microscopy (UEM) with femtosecond/picosecond (fs/ps) temporal resolution[1–4] has been used to inform a diverse and growing set of chemical, materials, and biological problems, such as phonon behaviors at atomic-to-nanoscale dimensions,[5–17] the spatiotemporal evolution of photoinduced phase transitions,[18–23] and the interaction of free electrons with photons at nanomaterial and biointerfaces.[24–35] High temporal resolution (*i.e.*, 100 fs to 1 ns) in UEM is typically achieved by interfacing a modified transmission electron microscope (TEM) with a fs pulsed laser such that stroboscopic photon-pump/electron-probe experiments can be conducted, though incorporation of an electromagnetic cavity or beam blanker into the column provides a laser-free (or hybrid) option with comparable temporal resolution.[36–47] With laser-driven UEM, however, spatial and temporal coherence of the probe electron packets quickly degrade with increasing density due to deleterious electron–electron interactions,[48–50] in addition to broadening effects imposed by electric and magnetic fields specific to the base TEM platform. This poses practical challenges to achieving high combined spatial, energy, and temporal resolutions for this form of ultrafast TEM, as a balance must be struck between signal acquisition time, electrons per packet and packets per unit time (*i.e.*, beam current), and specimen relaxation time ($\tau_{relaxation}$).

Methods for overcoming the resolution-limiting effects of electron–electron interactions in UEM focus on either undoing the broadening, as in proposed approaches employing pulse compression schemes,[51,52] or avoiding it altogether, as with conventional beams that are chopped or blanked (mentioned above), or by reducing the photoelectron packet density by simply using a lower pulsed-laser fluence.[1] Indeed, instrument-limited ~2 Å real-space resolution and sub-eV energy resolution have been demonstrated with both laser-free and laser-driven pulsed electron beams.[41,53,54] However, photoexcitation (or any type of triggering event) for stroboscopic study of dynamics requires extremely precise and highly robust spatial and temporal specimen reversibility. Accordingly, Å-resolved fs/ps real-space imaging of structural dynamics has yet to be demonstrated, despite the pulsed beams having sufficient coherence under certain operating conditions. As importantly, the high repetition rates (f) used to offset low packet densities and to reduce data acquisition times (true for both laser-driven and

Department of Chemical Engineering and Materials Science, University of Minnesota, 421 Washington Avenue SE, Minneapolis, MN, 55455, USA. E-mail: flan0076@umn.edu; Tel: +1-612-625-3867

laser-free approaches) relegates such high-f approaches to studies employing weak excitations (*i.e.*, small perturbations) or to events having approximately nanosecond or shorter lifetimes; more generally, to events where $\tau_{relaxation} < f^{-1}$.[4] Ideally, and especially for chemical and nanomaterials systems, one would identify an experimental parameter space where combined Å–fs–meV resolutions can be reached and preserved while being applied to the largest-possible set of phenomena and compositions (*i.e.*, the widest range of $\tau_{relaxation}$ for triggered events).

For fs laser-driven UEM, settings that lead to the (statistical) generation of a single photoelectron at the source (which is ideally collected into the illumination system[55]) should produce the most coherent beam at the highest beam current for a given f owing to the absence of electron–electron interactions.[1,56–58] Under such conditions, resolutions are then dictated by the fs laser-pulse properties and by space-charge-independent broadening effects inherent to the base TEM (*i.e.*, by fields specific to the instrument architecture, dimensions, materials, and geometries).[57–61] Accordingly, it would be useful to systematically study and quantify the impact of laser-pulse properties, electric and magnetic fields, and – importantly – specific instrument specifications on single-electron-packet resolutions, coherence, and collection efficiency in order to: (i) define theoretical limits, (ii) identify simple, low-cost approaches to tunable optimization, and (iii) begin to build-up a knowledge-base to better establish cause-effect relationships and to address unfounded dogma that has emerged where key data is missing.

Here, our contribution to a necessarily larger, multifaceted effort is a systematic set of simulations of single-electron-packet temporal distributions ($\tau_{electron}$) as a function of fs laser-pulse properties for the specific gun/accelerator architecture and dimensions of an FEI Tecnai Femto UEM (Thermo Fisher). Using the General Particle Tracer software package in tandem with field maps calculated using Poisson Superfish,[62,63] we studied the effects of easily-tunable laser-pulse properties and electron-gun dimensions on the temporal duration of single-electron packets. Adjustable parameters included the Wehnelt aperture diameter (D_W), the photoelectron emission spot size (*i.e.*, the fs UV probe-laser spot size on a truncated LaB_6 cathode), the laser photon energy ($h\nu$), the laser pulse duration (τ_{laser}), and the diameter of the cathode emitting surface (D_{tip}). In addition to identifying trends and uncovering unexpected behaviors, the goal here was to establish a foundation for additional systematic studies of increasing complexity for an entire laser-driven UEM system so as to ultimately generate an operational phase diagram for better targeting specific applications. While the simulations and results are specific to the Tecnai Femto system, the insights uncovered here are expected to be at least qualitatively applicable to other base TEM models and UEM systems.

Experimental

Elements of the simulations

General Particle Tracer (GPT, Pulsar Physics) was used to map particle trajectories through the electron gun and the electrostatic accelerator of a Thermo Fisher/FEI Tecnai Femto UEM (Fig. 1a).[63] To reduce computation time, simulations of n = 50 000 non-interacting electrons simultaneously generated from the cathode were performed. In the gun region, a series of dynodes comprise the accelerator and raise the electron energy to 200 keV. Once fully accelerated, the beam impinges upon an X-ray aperture, which here is the final element of the simulated electron gun. Two-dimensional, cylindrically-symmetric electrostatic field maps were calculated for the specific architecture and dimensions of the Tecnai Femto UEM (base instrument is Tecnai T20 G2)† using Poisson Superfish.[62]

In UEM mode, the electron gun consists of an unbiased Wehnelt triode with an aperture of diameter D_W and a truncated LaB_6 cathode with an emitting surface of diameter D_{tip} and a work function of Φ = 2.4 eV. The aperture can be variably positioned relative to the emitting surface at a distance Z_{tip} in the Wehnelt assembly. Here, a fixed Z_{tip} of 0.35 mm was used, as previous simulations of the Tecnai Femto indicated that this is the optimal position for maximizing electron collection efficiency in single-electron mode for D_W = 0.7 mm.[55] Further, a fixed Z_{tip} was used in order to specifically study the effects of photoemission spot size (*i.e.*, assumed to be the fwhm size of the laser spot on the LaB_6 surface) and D_W on $\tau_{electron}$. As with previous simulations on minimally-modified TEMs for ultrafast operation,[55] the effects of emission spot size and D_W are of interest because they are readily adjustable and tunable.

Single-electron packets were approximated by generating a set of non-interacting particles having momentum distributions and spatial coordinates specific to the photoemission characteristics under consideration. This approximates a series of single-electron photoemission events. Note the distinction between photoemission spot size and D_{tip}, which manifests in the emission probability (P) for a Gaussian laser-spot spatial profile (Fig. 1b). Further, LaB_6 shank emission was not considered, as the laser spot can be trained entirely on the flat cathode surface.[54,58] This is experimentally achieved by encircling the LaB_6 with a high Φ material such that $h\nu < \Phi$ and by simply focusing the laser-spot size such that it is smaller than D_{tip}.[1,8,58]

The probability of photoemission (P) was varied as the cosine of the initial emission angle, θ [*i.e.*, $P(\theta) = \cos(\theta)$] (Fig. 1c).[55,64] Note that different approaches to treating the angular photoemission distribution in UEM and ultrafast electron diffraction (UED) simulations have been adopted. One common approach is to assume a uniform distribution of photoemission probabilities within the hemisphere subtended by the photocathode emitting surface.[57,59,65] Compared to the $\cos(\theta)$ approach, uniformly-distributed trajectories will produce photoelectron packets with increased temporal distortions due to the larger fraction of off-axis emission events. Only the $\cos(\theta)$ distribution was employed here. Following this, the product of the Lorentz factor (γ) and the normalized relativistic velocity (β) was used as the momentum factor ($\gamma\beta$) to initialize the GPT simulations.

Initial photoelectron kinetic-energy distributions were modeled as calculated transmission coefficients for free electrons

† Provided by Dr Erik Kieft of Thermo Fisher Scientific.

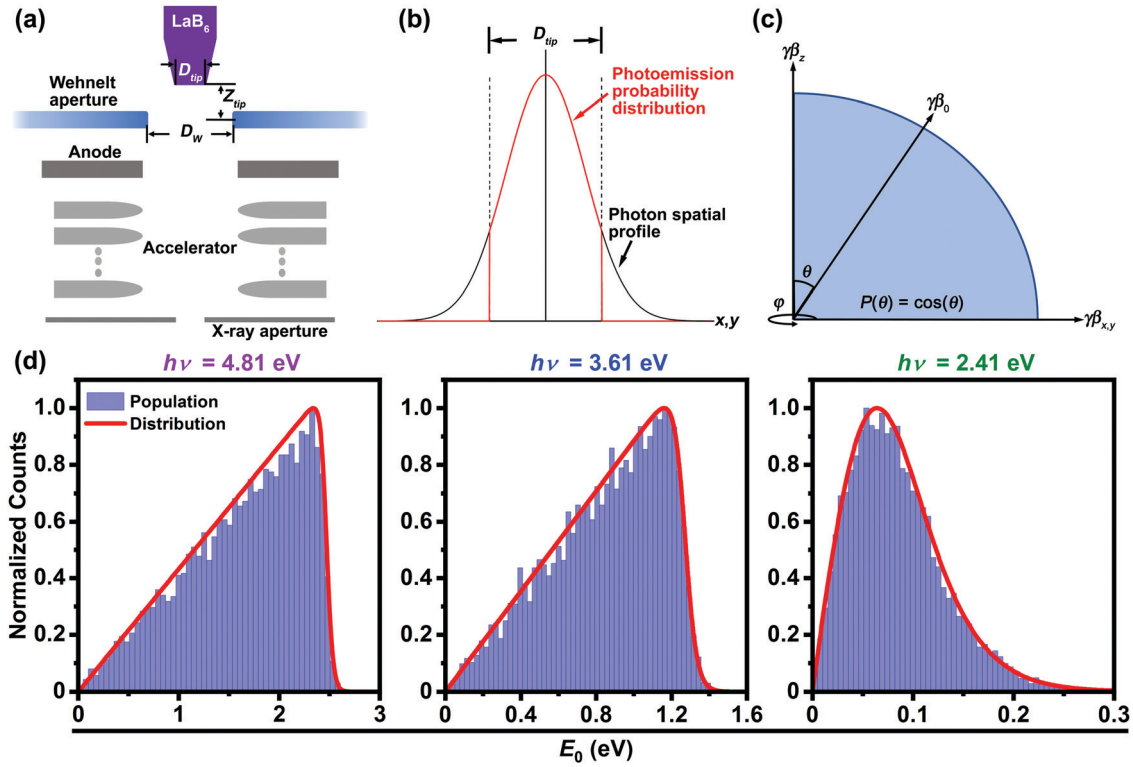

Fig. 1 Elements of the simulations. (a) Simplified schematic of the FEI Tecnai Femto electron gun and accelerator with key components and dimensions labeled. D_{tip} is the diameter of the LaB_6 emitting surface, Z_{tip} is the distance from the LaB_6 surface to the plane of the Wehnelt aperture (here, fixed at 0.35 mm), and D_W is the diameter of the Wehnelt aperture. (b) Spatial photoelectron emission probability (red curve) from the LaB_6 emitting surface for a Gaussian laser-spot shape (black curve). The probability is set to zero for $x,y > D_{tip}$. (c) Photoelectron emission probability (P) as a function of emission angle (θ) relative to the center of the illuminated LaB_6 surface. The full probability distribution subtended by the LaB_6 emitting surface parallel to the x,y plane is generated by sweeping azimuthally over φ to establish cylindrical symmetry. γ and β are the Lorentz factor and the normalized relativistic velocity, respectively. The product $\gamma\beta$ is the rest-mass-normalized particle momentum used in GPT. (d) Calculated initial probe photoelectron kinetic-energy (E_0) distributions (red curves) for LaB_6 with work function Φ = 2.4 eV and select photon energies $h\nu$ = 4.81 (left), 3.61 (center), and 2.41 eV (right) (*i.e.*, harmonics of the Yb:KGW fs laser in the UEM lab at Minnesota).

encountering a step potential (Fig. 1d). Photoemission was approximated by shifting the Fermi–Dirac distribution by the amount of the incident photon energy $h\nu$; the three photon energies studied here (2.41, 3.61, and 4.81 eV) are harmonics (2nd–4th, respectively) of the UEM laser system at Minnesota (Yb:KGW, $h\nu_{fundamental}$ = 1.2 eV). Note that this approach is an approximation for near-threshold photoemission from the surface of LaB_6.[66] All reported single-electron-packet properties are those that are present 2.5 ns after photoemission. This ensured that all packets were fully increased to 200 keV and had reached the X-ray aperture, regardless of initial trajectory. Finally, $\tau_{electron}$ (single-electron temporal distribution for n individual, integrated non-interacting particles) was calculated by dividing the root-mean-square longitudinal packet length by the average longitudinal velocity.

Results and discussion

Dependence of $\tau_{electron}$ on photoemission spot size and E_0 for key values of D_W

To establish a baseline behavior for $\tau_{electron}$, three discrete values of E_0 were first simulated (0.10, 1.76, and 2.40 eV) for two Wehnelt aperture diameters (0.7 and 1.0 mm, Fig. 2). These E_0 values were selected because 0.10 and 2.4 eV are near the extremes of the full range of E_0 for the oft-used $h\nu$ = 4.8 eV and Φ = 2.4 eV for generating photoelectrons in UEM experiments, while 1.76 eV is the average value of the calculated distribution for $h\nu$ = 4.81 eV (Fig. 1d, left panel). The two values of D_W were chosen because they are standard (0.7 mm) and optimum (1.0 mm) diameters used in thermionic and single-electron UEM modes (per simulation), respectively.[55] Because the particles in each bunch are non-interacting, one can separate the space-charge-independent broadening effects for different values of E_0. Further, the use of single, discrete values of E_0 at this stage, rather than the distributions shown in Fig. 1d, provides direct insight into the degree of influence of those effects.

The simulations indicate that a strong dependence of $\tau_{electron}$ on photoemission spot size exists for D_W = 1.0 mm as compared to the standard 0.7 mm aperture, which instead shows very little variation across the entire range of spot sizes investigated (0–180 μm). In particular, the two larger E_0 values (*i.e.*, larger initial kinetic energies due to larger $h\nu$ values) for D_W = 1.0 mm show a large drop in $\tau_{electron}$ to near the

laser-pulse duration (τ_{laser} = 300 fs) with decreasing spot size. This is intriguing because it suggests that experimental parameter space exists wherein one can overcome degraded temporal resolution for cases where $h\nu > \Phi$ when using a tightly-focused laser. Further, the simulated value of $\tau_{electron}$ is approximately the same for all values of E_0 at spot sizes smaller than ~20 μm (Fig. 2, bottom panel). This suggests that one might be able to both preserve optimum temporal resolution while also increasing photoemission probability when operating in the single-electron regime. However, it is important to note that the behaviors and thus optimum settings will change when each laser pulse produces multiple photoelectrons and electron–electron interactions are present. Again, throughout this study we focused solely on the idealized single-electron regime, but work is needed to better understand the behaviors of packets with increasing density generated with fs laser pulses. It should be noted that the general increase in $\tau_{electron}$ with E_0 (*i.e.*, $h\nu$), which is especially apparent for D_W = 0.7 mm, is a well-known effect in UED experiments. The simulations here indicate this effect is also present in UEM, despite the more complex instrument architecture. However, this increased complexity may also offer additional flexibility for offsetting negative effects with simple adjustments to key components once the parameter space is mapped, as suggested by the results in Fig. 2.

The effect of photoemission spot size on $\tau_{electron}$ shown in Fig. 2 is due in part to the precise trajectories of the photoelectrons in the gun region. Integrated over n electrons, larger emission spot sizes will have a larger fraction of off-optical-axis particles, which then leads to broadening of the temporal distribution. Photoelectrons emitted from surface regions that are far from the optical axis, as well as those that are not parallel to the axis when emitted, will contribute to the broadening due to prolonged dwell times and delays in acceleration. Importantly, the Wehnelt aperture is the main electrostatic component affecting tip-region dwell time, with the diameter (D_W) strongly impacting overall behavior and thus serving as a source of tunability and optimization. This is intuitively straightforward to understand. Decreasing D_W effectively moves the associated electrostatic field closer to the optical axis, thus impacting a larger fraction of the total (integrated) emitted population and increasing the sensitivity of $\tau_{electron}$ to off-axis and non-parallel photoelectrons. The D_W = 1.0 mm data in Fig. 2 further illustrate this effect; photoemission spots below a certain diameter dictated by the specific D_W will have minimally-impacted populations. Thus, the onset of an increase in $\tau_{electron}$ will move to larger spot sizes as D_W is also increased.

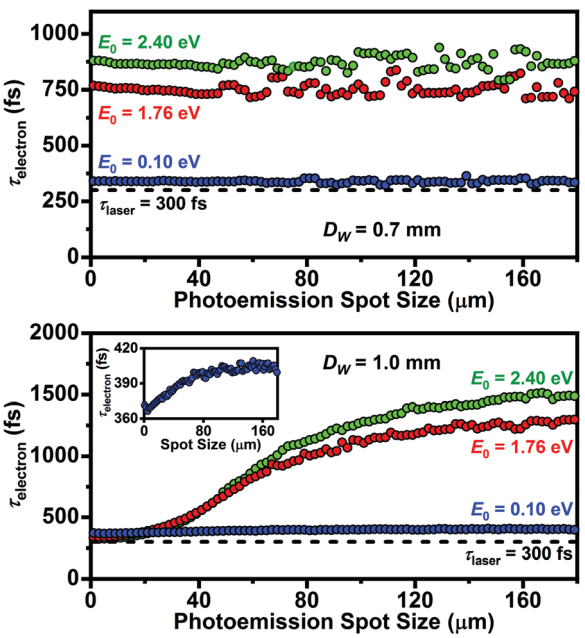

Fig. 2 Single-electron-packet duration ($\tau_{electron}$; fwhm) as a function of LaB_6 photoemission spot size for D_W = 0.7 mm (top) and D_W = 1.0 mm (bottom). Note that three discrete initial photoelectron kinetic energies (E_0 = 0.10, 1.76, and 2.40 eV) were compared (*i.e.*, here, the full distributions shown in Fig. 1d were not yet used in order to first focus on the effect of photoemission spot size and D_W). The horizontal black dashed line in each panel (τ_{laser}) represents the selected probe laser-pulse duration of 300 fs (fwhm) typical of the current system at Minnesota. The inset (bottom panel) is the 0.10 eV plot for D_W = 1.0 mm with the *y*-axis rescaled to visualize the subtle response of $\tau_{electron}$.

Unlike the 1.0 mm aperture, the standard 0.7 mm aperture appears to impact all photoelectrons regardless of emission spot size. Practically, this may be beneficial, as one need not worry about carefully controlling spot size in order to have a consistent $\tau_{electron}$. However, it does not provide for simple tunability or for reaching resolutions close to τ_{laser} beyond using lower $h\nu$ (at the expense of beam current for a given f). Relatedly, temporal distortions of electron packets have been indirectly observed for UEM systems having independent control over Wehnelt bias and for photoelectrons emitted from shank regions of conical cathodes for reasons similar to those here, though differences in magnitude are potentially due to differing geometries and to the absence of electron–electron interactions in the simulations.[54,60] Such distortions are also not unlike those introduced by magnetic lenses.[65,67,68]

The increase in $\tau_{electron}$ with $h\nu$ (Fig. 2) can be explained as follows. One contribution comes from the distribution of initial trajectories, which will create an effective dispersion in the longitudinal velocities. This will result in a general statistical broadening of the temporal distribution due to electron acceleration.[57,59] However, the effect will diminish with decreasing E_0 due to the lower initial velocities. Another related contribution comes from the resulting variation in electron-gun dwell times (*i.e.*, the time needed for each electron to reach a fixed position after the final electron-gun element). Importantly, the difference in dwell time between the extremes in initial trajectory (θ = 0 and $\frac{\pi}{2}$, Fig. 1c) increases with increasing E_0. For example, for E_0 = 0.10 eV the spread in dwell time increases 500 fs for θ increasing from 0 to $\frac{\pi}{2}$, but over the same trajectory range, it increases by 2.6 ps for E_0 = 2.40 eV (Fig. 3). More generally, electron packets with larger E_0 will, on average, have a shorter dwell time (*i.e.*, shorter arrival time) relative to smaller E_0 at any given trajectory within the relevant range despite the non-linear behavior. It is important to note

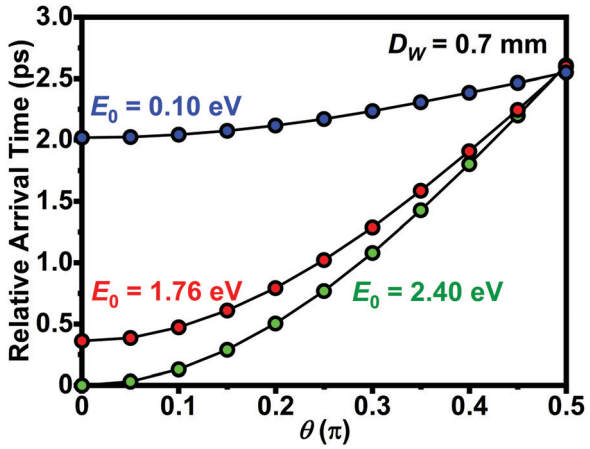

Fig. 3 Relative photoelectron arrival time at a fixed position after the final electron-gun element as a function of initial photoemission angle from the LaB_6 surface (θ) for D_W = 0.7 mm and E_0 = 0.10, 1.76, and 2.40 eV. The photoemission spot size was fixed at 5 μm diameter for all data, and all photoelectrons had the same initial momentum. All arrival times are relative to θ = 0 (*i.e.*, parallel to the optical axis) and E_0 = 2.40 eV, the specific condition for which the shortest transit time to the aperture occurs.

that the dwell-time delay is not due to electrostatic accelerator-induced broadening, because all electrons are emitted with identical longitudinal velocities. Instead, it is a result of the increased interactions of large-angle trajectories with the Wehnelt aperture for larger E_0.

Systematic study of the effect of D_W on $\tau_{electron}$ for an $h\nu$-driven distribution of E_0

The results discussed above, which provide a foundation upon which to increase the complexity of the simulations, have significant implications for n photoelectrons comprising a temporally-integrated packet consisting of a range of E_0 (Fig. 1d) rather than a single discrete value. Accordingly, Fig. 4

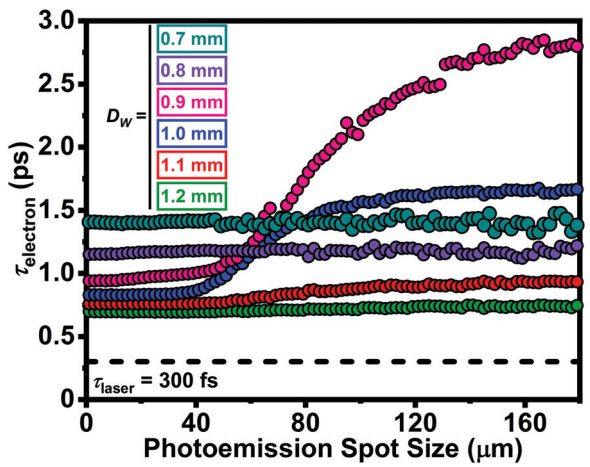

Fig. 4 Single-electron packet duration ($\tau_{electron}$, fwhm) as a function of photoemission spot size for D_W ranging 0.7–1.2 mm. The LaB_6 D_{tip} was 180 μm. The horizontal black dashed line (τ_{laser}) represents the selected probe laser-pulse duration of 300 fs (fwhm). The $h\nu$ = 4.81 eV distribution in Fig. 1d was used as the E_0.

summarizes the results of such simulations, where the E_0 distribution for the $h\nu$ = 4.81 eV case shown in Fig. 1d was used instead of the discrete value E_0 = 2.40 eV (Fig. 2 and 3). Further, the simulations were performed for six different D_W ranging 0.7–1.2 mm, all as a function of the photoemission spot size.

Several notable behaviors emerge from the simulations summarized in Fig. 4. Perhaps the most notable is that, for spot sizes smaller than ~50 μm, $\tau_{electron}$ decreases with increasing D_W, reaching a value of ~700 fs (fwhm) for the largest aperture (again, for the broadest E_0 distribution generated from $h\nu$ = 4.81 eV with τ_{laser} = 300 fs). This again indicates that D_W is an adjustable parameter for optimizing temporal resolution of minimally-modified thermionic UEM systems that lack independent control over Wehnelt bias. As is the case for discrete values of E_0 (Fig. 2), this effect is due to a reduction in the influence of Wehnelt electrostatic fields on off-axis photoelectrons [emphasizing again the $P(\theta) = \cos(\theta)$ distribution used here]. Interestingly, there is a rather abrupt onset of aperture influence on $\tau_{electron}$ dispersion with photoemission spot size when increasing from D_W = 0.8 to 0.9 mm, with a nearly similarly-abrupt relaxation when increasing from 1.0 to 1.1 mm (though a relatively modest dispersion of ~100 fs is still seen for D_W = 1.1 mm). At least with respect to $\tau_{electron}$, the simulations indicate that a D_W larger than ~1 mm provides the highest temporal resolution (for a given D_W) combined with the least sensitivity to photoemission spot size. Further, the sensitivity of $\tau_{electron}$ to spot size for D_W = 0.9 and 1.0 mm is connected to the cosine functional form of emission probability (Fig. 1c) and, therefore, the precise (integrated) distribution of photoelectron kinetic energies (Fig. 1d).

Compared to data shown in Fig. 2 (*i.e.*, compared to E_0 = 2.40 eV for each D_W), the single-electron packets generated from a distribution of E_0 shown in Fig. 4 are generally further temporally broadened. This is due to a further increase in longitudinal-velocity spread and broadening of the associated distribution in electron-gun dwell times (see Fig. 3 for the case of discrete values of E_0). Such broadening typically manifests in energy and longitudinal-velocity distributions of single electrons propagating in accelerating fields.[59,61] Here, however, the effect appears to also emerge in non-accelerating fields due to the electrostatic forces imposed by an unbiased Wehnelt aperture and the portion of the E_0 distribution that dominates the overall behavior for specific combinations of non-zero photoemission spot sizes and D_W. Indeed, the effect becomes quite deleterious in terms of $\tau_{electron}$ for standard D_W aperture sizes (*e.g.*, 0.7 mm), regardless of spot size; here, $\tau_{electron}$ is broadened to 1.4 ps from the laser limit, despite the general shortened dwell time for higher-energy photoelectrons (Fig. 3).

Simulations of E_0 ($h\nu$) distributions for select D_W

As Fig. 4 summarizes the behavior of $\tau_{electron}$ as a function of photoemission spot size for various D_W and for the $h\nu$ = 4.81 eV distribution of E_0 (Fig. 1d), a systematic approach dictates that simulations for the other two select E_0 distributions (again, as specified by the available laser harmonics) also be performed and compared. Accordingly, Fig. 5 summarizes the results for

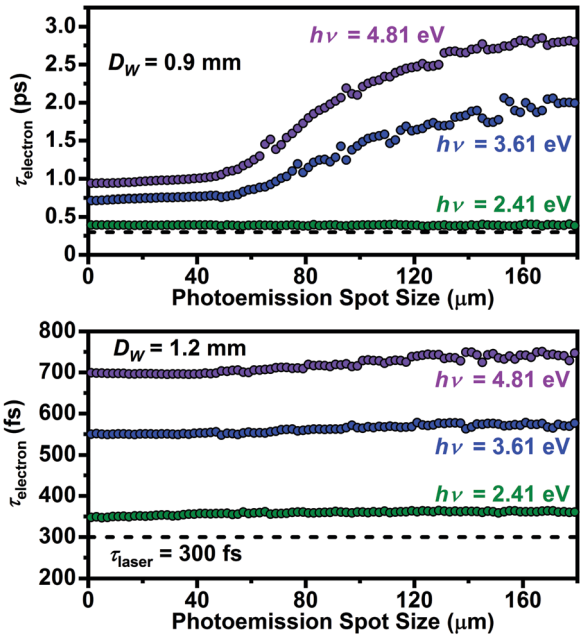

Fig. 5 Single-electron packet duration ($\tau_{electron}$, fwhm) as a function of photoemission spot size for discrete laser photon energies ($h\nu$ = 2.41, 3.61, and 4.81 eV) for D_W = 0.9 mm (top) and 1.2 mm (bottom). The LaB_6 D_{tip} was 180 μm. The horizontal black dashed line (τ_{laser}) in each panel represents the selected probe laser-pulse duration of 300 fs (fwhm). The E_0 distributions shown in Fig. 1d were used for each corresponding photon energy.

D_W = 0.9 and 1.2 mm for all three E_0 distributions. These aperture values were chosen because they show (for the E_0 = 2.41 eV distribution; Fig. 4) the strongest dispersion, in the case of the 0.9 mm aperture, and the weakest and mostly-insensitive temporal broadening (*i.e.*, the best temporal resolution that is robust across all spot sizes), in the case of the 1.2 mm aperture.

As can be seen, the trend for E_0 = 2.41 eV (*i.e.*, $h\nu$ = 4.81 eV) generally continues for the other distributions with some notable and important variations. Photoexcitation with $h\nu$ closer to the LaB_6 Φ value (here, fixed at 2.4 eV) produces an overall improvement in $\tau_{electron}$ for both values of D_W, regardless of photoemission spot size. Further, the strong dispersion seen for D_W = 0.9 mm and $h\nu$ = 4.81 eV is also observed for $h\nu$ = 3.61 eV (scales approximately linearly) but is relaxed across all spot sizes for $h\nu$ = 2.41 eV (*i.e.*, $h\nu$ approximately equivalent to Φ). Indeed, $\tau_{electron}$ for $h\nu$ = 2.41 eV is broadened by ~50 fs (17%) relative to τ_{laser} across all spot sizes for both values of D_W (again, however, such a condition would introduce practical challenges with beam current and thus f).

Generally, a decrease in $\tau_{electron}$ as $h\nu$ approaches Φ is expected, as both the total integrated energy and the overall energy spread of the photoelectron distribution are reduced (see Fig. 1d).[61,67] Despite the differing architectures, dimensions, and field strengths, such an effect also exists in dedicated UED instruments and arises from the dependence on the longitudinal velocity spread and the average field strength of the accelerating cavity (which here is 1.7 kV mm^{-1}).[59] Further, the longitudinal velocity spread depends upon E_0 and the angular distributions of the photoelectrons. Here the specific accelerator-induced temporal broadening was calculated to be 650 fs for $h\nu$ = 4.81 eV, 474 fs for $h\nu$ = 3.61 eV, and 171 fs for $h\nu$ = 2.41 eV. Convoluting this with τ_{laser} (root sum square), the minimum $\tau_{electron}$ for D_W = 1.2 mm was found to be 716, 561, and 345 fs (fwhm) for $h\nu$ = 4.81, 3.61, and 2.41 eV, respectively (spot size = 0, Fig. 5 bottom panel). For D_W = 0.9 mm, the minimum $\tau_{electron}$ increases by ~200 fs for 4.81 and 3.61 eV and by ~50 fs for 2.41 eV due to increased interactions with the Wehnelt aperture for a larger fraction of the overall integrated photoelectron distribution.

Though not the subject of this particular study, it is worth briefly emphasizing that one must also consider the impact of the laser-pulse properties and instrument architecture on beam coherence and beam current (*i.e.*, photoelectron collection efficiency) for studying ultrafast dynamics with Å–fs–meV TEM (in addition to $\tau_{relaxation}$ and reversibility). For example, using $h\nu$ = Φ may generally provide the highest coherence and shortest $\tau_{electron}$ (*i.e.*, best temporal resolution), but it will also result in the lowest photoelectron yield and the lowest beam current.[69] This poses a challenge, as long acquisition times and/or high repetition rates must be used in order to minimize signal acquisition times and the deleterious impacts of lab and instrument instabilities. To offset the low beam current, one can use a higher laser fluence when $h\nu$ is close to Φ, but this introduces other challenges due to electron–electron interactions and associated reductions in coherence and $\tau_{electron}$ and will negate any gains achieved by matching $h\nu$ to Φ. The view here is that $\tau_{electron}$ is one of three important parameters that need to be quantitatively understood, the other two being coherence and current, and they are all interwoven with one another. Thus, generation of operational phase diagrams for these parameters for specific instruments should be coupled with specific lab conditions in order to define ultimate resolution limits. This is likely to require multiple systematic studies of increasing complexity, which are then tested with careful experimentation under optimal conditions.

Effect of τ_{laser} on $\tau_{electron}$

In addition to $h\nu$, the laser-pulse duration (τ_{laser}) for photoelectron-generation was a specific parameter studied here. As optimization and trends of $\tau_{electron}$ were the focus, values of τ_{laser} < 300 fs were studied, as it was hypothesized that shorter τ_{laser} will generally lead to shorter $\tau_{electron}$. Indeed, as noted above, in the single-electron regime, temporal resolution is expected to be directly impacted by laser parameters, including τ_{laser}. Accordingly, Fig. 6 summarizes the results for τ_{laser} ranging 50 to 300 fs at 50 fs steps. Otherwise identical conditions to those for Fig. 4 were used, where the E_0 distribution for $h\nu$ = 4.81 eV was simulated (Fig. 1d).

The immediate and most important result shown in Fig. 6 is that, even for the shortest τ_{laser} = 50 fs, the minimum $\tau_{electron}$ observed is broadened by several hundred fs (*e.g.*, $\tau_{electron}$ = 625 fs at ~20 μm spot size for D_W = 1.2 mm, Fig. 6c). This suggests that simply using a shorter fs laser pulse is insufficient for significantly improving UEM temporal resolution in the single-electron regime. This stems from the influence the

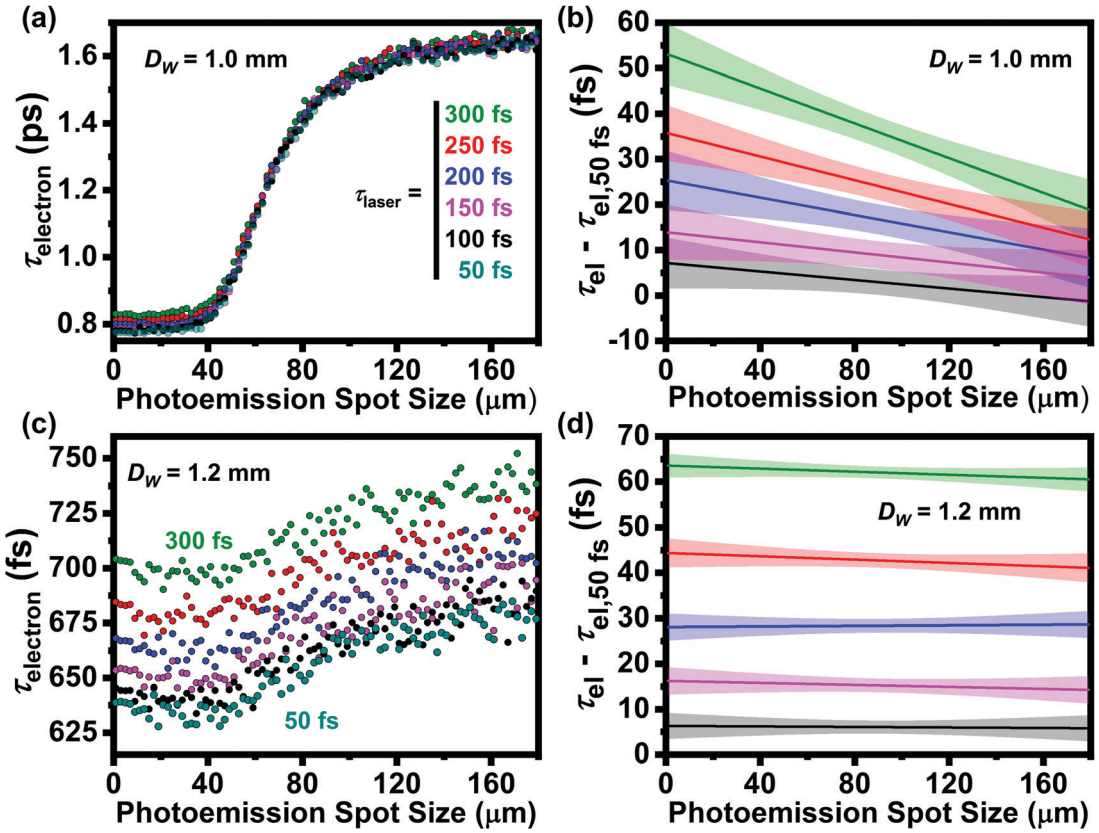

Fig. 6 Single-electron packet duration ($\tau_{electron}$, fwhm) as a function of photoemission spot size for laser-pulse durations (τ_{laser}, fwhm) spanning 50 to 300 fs (panel a legend for τ_{laser} applies to all panels) for D_W of 1.0 mm (a and b) and 1.2 mm (c and d). D_{tip} = 180 μm and the E_0 distribution for $h\nu$ = 4.81 eV (Fig. 1d) were used for all simulations. Panels (b and d) show linear fits to the difference between $\tau_{electron}$ (*i.e.*, τ_{el}) for τ_{laser} = 50 fs ($\tau_{el} - \tau_{el,50\ fs}$) and all other laser-pulse durations for D_W = 1.0 and 1.2 mm, respectively. The shaded bands around each line represent the 95% confidence level.

Wehnelt aperture and electrostatic interactions have on $\tau_{electron}$, as observed when comparing the results for D_W = 1.0 and 1.2 mm (*e.g.*, much larger dispersion for the smaller aperture). This dispersion seems to be a general limitation to $\tau_{electron}$, despite the complete absence of electron–electron interactions in the single-electron regime.[67] Fig. 6 also shows that, while improvement in $\tau_{electron}$ occurs when reducing τ_{laser} from 300 to 50 fs (regardless of D_W), shorter laser-pulse durations result in diminishing returns in temporal resolution. For example, for D_W = 1.2 mm, the minimum $\tau_{electron}$ is ~690 fs for τ_{laser} = 300 fs, compared to 625 fs for τ_{laser} = 50 fs. One must also contend with larger spectral bandwidths at shorter τ_{laser} and the associated impacts on $\tau_{electron}$, in addition to challenges imposed by electrostatic effects. The effect of diminishing returns when going to shorter τ_{laser} is summarized in Fig. 6b and d, where the difference between τ_{laser} = 50 fs and all other durations is plotted as a function of the photoemission spot size.

Effect of LaB_6 tip size (D_{tip}) on $\tau_{electron}$

Finally, the diameter of the emitting surface of the truncated LaB_6 cathode (D_{tip}) was another adjustable parameter explored here owing to the hypothesized influence different tip sizes will have on the electrostatic fields in the gun region. The effects of four commonly-used D_{tip} on $\tau_{electron}$ as a function of photoemission spot size were investigated (Fig. 7). For each simulation, D_W was fixed at 1.0 mm, the E_0 distribution for $h\nu$ = 4.81 eV was used (Fig. 1d), and τ_{laser} was fixed at 300 fs (fwhm). It was found that D_{tip} generally has a significant effect on $\tau_{electron}$, though the magnitude and sensitivity strongly depend on the photoemission spot size. Indeed, at a spot size of ~10 μm, $\tau_{electron}$ is roughly identical for all D_{tip} (~850 fs), but increasing to 16 μm (the limit of the smallest tip) causes $\tau_{electron}$ for D_{tip} = 50 μm to increase to nearly 1.25 ps. Further, $\tau_{electron}$ varies by nearly a factor of two for the three largest tip sizes at a fixed spot size of 35 μm. This behavior supports the hypothesis that the tip size itself impacts the electrostatic fields in the gun region, which in turn influences $\tau_{electron}$. This is practically important, as it indicates $\tau_{electron}$ may significantly change if the tip size is changed (*e.g.*, by changing cathodes) but the laser spot size is not (*e.g.*, by changing the focal spot size). Moving to larger spot sizes, the dispersion behavior is such that $\tau_{electron}$ plateaus to a single value, as observed for many cases above, suggesting a relatively poor but consistent temporal resolution can be expected for D_{tip} > ~150 μm. In general, the results indicate the dispersion behavior is such that variations in $\tau_{electron}$ are initially small for tight laser focus which then passes through a strongly-dispersive regime before again plateauing an elevated but consistent and robust value for large spot sizes. The trend in Fig. 7 also suggests that the strongly-dispersive regime will shift to larger spot sizes for

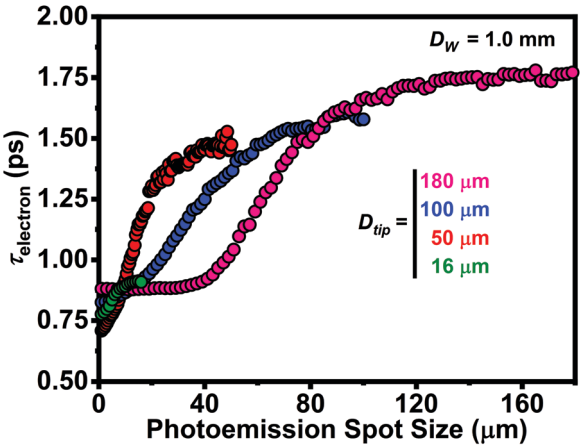

Fig. 7 Dependence of $\tau_{electron}$ (fwhm) on photoemission spot size for four LaB_6 emitting surface diameters (D_{tip} = 16, 50, 100, and 180 μm). Wehnelt diameter was fixed at D_W = 1.0 mm, the incident laser-pulse duration was fixed at τ_{laser} = 300 fs (fwhm), and the E_0 distribution for $h\nu$ = 4.81 eV shown in Fig. 1d was used each D_{tip}. Photoemission spot sizes were limited to the available emitting surface (*i.e.*, shank emission for spot sizes larger than D_{tip} were ignored, as justified by the reasons given above).

larger D_{tip} (compare the 100 and 180 μm simulations). This suggests that a practical approach to preserving high temporal resolution while having a somewhat forgiving spot-size requirement would be to use a large cathode and a laser spot size that is smaller than that at which the dispersion sets in (*i.e.*, smaller than the tip-dependent threshold dispersion value).

In summary, we have systematically explored the impact of various laser-pulse and electron-gun conditions and parameters on the duration of single-electron packets using GPT simulations and properties specific to the FEI Tecnai Femto UEM. We have identified a number of simple, adjustable parameters for optimizing the temporal resolution, and we have also identified operating phase spaces of both low and high sensitivity to those parameters. This work constitutes one part of a larger effort aimed at quantifying the ultimate spatial, temporal, and energy resolutions of ultrafast TEMs such that combined Å–fs–meV operating conditions might be achieved and experimentally demonstrated. This foundational effort, wherein temporal resolution under space-charge-free conditions was explored, will complement studies focused on understanding beam coherence and beam current in order to conduct multi-dimensional parameter-space mapping. An additional hope is that this work will continue to spur significant efforts into expanding TEM temporal resolution at levels comparable to spatial and energy resolutions.

Author contributions

W. A. C. contributions were data curation, formal analysis, investigation, methodology, software, validation, visualization, writing – original draft, writing – review and editing. D. J. F. contributions were conceptualization, data curation, funding acquisition, methodology, project administration, resources, supervision, visualization, writing – original draft, writing – review and editing. See the NISO CRediT taxonomy for definitions of contributing roles (credit.niso.org).

Conflicts of interest

There are no conflicts to declare.

Acknowledgements

This material is based on work supported by the U.S. Department of Energy, Office of Science, Office of Basic Energy Sciences under Award No. DE-SC0018204. This material is based upon work supported by the National Science Foundation Graduate Research Fellowship Program under Grant No. DGE-1839286. This work was supported partially by the National Science Foundation through the University of Minnesota MRSEC under Award Number DMR-2011401. Acknowledgement is made to the Donors of the American Chemical Society Petroleum Research Fund for partial support of this research under Award No. 60584-ND10. We thank Dr Erik Kieft of Thermo Fisher Scientific for assistance with modeling the FEI Tecnai Femto architecture and for ensuring accurate electrostatic field maps were generated.

References

1 V. A. Lobastov, R. Srinivasan and A. H. Zewail, *Proc. Natl. Acad. Sci. U. S. A.*, 2005, **102**, 7069–7073.
2 A. H. Zewail, *Science*, 2010, **328**, 187–193.
3 D. J. Flannigan and A. H. Zewail, *Acc. Chem. Res.*, 2012, **45**, 1828–1839.
4 D. A. Plemmons, P. K. Suri and D. J. Flannigan, *Chem. Mater.*, 2015, **27**, 3178–3192.
5 A. Yurtsever and A. H. Zewail, *Proc. Natl. Acad. Sci. U. S. A.*, 2011, **108**, 3152–3156.
6 A. Yurtsever, S. Schaefer and A. H. Zewail, *Nano Lett.*, 2012, **12**, 3772–3777.
7 D. R. Cremons, D. A. Plemmons and D. J. Flannigan, *Nat. Commun.*, 2016, **7**, 11230.
8 D. T. Valley, V. E. Ferry and D. J. Flannigan, *Nano Lett.*, 2016, **16**, 7302–7308.
9 D. R. Cremons, D. X. Du and D. J. Flannigan, *Phy. Rev. Mater.*, 2017, **1**, 073801.
10 D. R. Cremons, D. A. Plemmons and D. J. Flannigan, *Struct. Dyn.*, 2017, **4**, 044019.
11 A. J. McKenna, J. K. Eliason and D. J. Flannigan, *Nano Lett.*, 2017, **17**, 3952–3958.
12 A. Feist, N. Rubiano da Silva, W. Liang, C. Ropers and S. Schäfer, *Struct. Dyn.*, 2018, **5**, 014302.
13 Y. C. Zhang and D. J. Flannigan, *Nano Lett.*, 2019, **19**, 8216–8224.
14 S. A. Reisbick, Y. C. Zhang and D. J. Flannigan, *J. Phys. Chem. A*, 2020, **124**, 1877–1884.

15 A. Nakamura, T. Shimojima, Y. Chiashi, M. Kamitani, H. Sakai, S. Ishiwata, H. Li and K. Ishizaka, *Nano Lett.*, 2020, **20**, 4932–4938.
16 E. J. VandenBussche and D. J. Flannigan, *Philos. Trans. R. Soc., A*, 2020, **378**, 20190598.
17 Y. Kurman, R. Dahan, H. H. Sheinfux, K. Wang, M. Yannai, Y. Adiv, O. Reinhardt, L. H. G. Tizei, S. Y. Woo, J. Li, J. H. Edgar, M. Kociak, F. H. L. Koppens and I. Kaminer, *Science*, 2021, **372**, 1181–1186.
18 M. S. Grinolds, V. A. Lobastov, J. Weissenrieder and A. H. Zewail, *Proc. Natl. Acad. Sci. U. S. A.*, 2006, **103**, 18427–18431.
19 V. A. Lobastov, J. Weissenrieder, J. Tang and A. H. Zewail, *Nano Lett.*, 2007, **7**, 2552–2558.
20 S. Z. Ji, O. Granas, K. Rossnagel and J. Weissenrieder, *Phys. Rev. B*, 2020, **101**, 094303.
21 X. Fu, F. Barantani, S. Gargiulo, I. Madan, G. Berruto, T. LaGrange, L. Jin, J. Wu, G. M. Vanacore, F. Carbone and Y. Zhu, *Nat. Commun.*, 2020, **11**, 5770.
22 T. Danz, T. Domrose and C. Ropers, *Science*, 2021, **371**, 371–374.
23 S. A. Reisbick, Y. Zhang, J. Chen, P. E. Engen and D. J. Flannigan, *J. Phys. Chem. Lett.*, 2021, **12**, 6439–6447.
24 B. Barwick, D. J. Flannigan and A. H. Zewail, *Nature*, 2009, **462**, 902–906.
25 D. J. Flannigan, B. Barwick and A. H. Zewail, *Proc. Natl. Acad. Sci. U. S. A.*, 2010, **107**, 9933–9937.
26 A. Yurtsever, J. S. Baskin and A. H. Zewail, *Nano Lett.*, 2012, **12**, 5027–5032.
27 A. Yurtsever, R. M. van der Veen and A. H. Zewail, *Science*, 2012, **335**, 59–64.
28 A. Yurtsever and A. H. Zewail, *Nano Lett.*, 2012, **12**, 3334–3338.
29 S. T. Park, A. Yurtsever, J. S. Baskin and A. H. Zewail, *Proc. Natl. Acad. Sci. U. S. A.*, 2013, **110**, 9277–9282.
30 B. Barwick and A. H. Zewail, *ACS Photonics*, 2015, **2**, 1391–1402.
31 T. T. A. Lummen, R. J. Lamb, G. Berruto, T. LaGrange, L. Dal Negro, F. J. G. de Abajo, D. McGrouther, B. Barwick and F. Carbone, *Nat. Commun.*, 2016, **7**, 13156.
32 M. Kaplan, B. K. Yoo, J. Tang, T. E. Karam, B. L. Liao, D. Majumdar, D. Baltimore, G. J. Jensen and A. H. Zewail, *Angew. Chem., Int. Ed.*, 2017, **56**, 11498–11501.
33 Y. Lu, B. K. Yoo, A. H. C. Ng, J. Kim, S. Yeom, J. Tang, M. M. Lin, A. H. Zewail and J. R. Heath, *Proc. Natl. Acad. Sci. U. S. A.*, 2019, **116**, 22014–22019.
34 A. Konecna, V. Di Giulio, V. Mkhitaryan, C. Ropers and F. J. G. de Abajo, *ACS Photonics*, 2020, **7**, 1290–1296.
35 M. Liebtrau, M. Sivis, A. Feist, H. Lourenco-Martins, N. Pazos-Perez, R. A. Alvarez-Puebla, F. J. G. de Abajo, A. Polman and C. Ropers, *Light: Sci. Appl.*, 2021, **10**, 82.
36 A. Lassise, P. H. A. Mutsaers and O. J. Luiten, *Rev. Sci. Instrum.*, 2012, **83**, 043705.
37 J. Q. Qiu, G. H. Ha, C. G. Jing, S. V. Baryshev, B. W. Reed, J. W. Lau and Y. M. Zhu, *Ultramicroscopy*, 2016, **161**, 130–136.
38 W. Verhoeven, J. F. M. van Rens, E. R. Kieft, P. H. A. Mutsaers and O. J. Luiten, *Ultramicroscopy*, 2018, **188**, 85–89.
39 J. F. M. van Rens, W. Verhoeven, J. G. H. Franssen, A. C. Lassise, X. F. D. Stragier, E. R. Kieft, P. H. A. Mutsaers and O. J. Luiten, *Ultramicroscopy*, 2018, **184**, 77–89.
40 J. F. M. van Rens, W. Verhoeven, E. R. Kieft, P. H. A. Mutsaers and O. J. Luiten, *Appl. Phys. Lett.*, 2018, **113**, 163104.
41 C. Kisielowski, P. Specht, B. Freitag, E. R. Kieft, W. Verhoeven, J. F. M. van Rens, P. Mutsaers, J. Luiten, S. Rozeveld, J. Kang, A. J. McKenna, P. Nickias and D. F. Yancey, *Adv. Funct. Mater.*, 2019, **29**, 1807818.
42 C. G. Jing, Y. M. Zhu, A. Liu, K. Schliep, X. W. Fu, Y. B. Zhao, E. Montgomery, W. Rush, A. Kanareykin, M. Katz and J. Lau, *Ultramicroscopy*, 2019, **207**, 112829.
43 I. G. C. Weppelman, R. J. Moerland, L. Zhang, E. Kieft, P. Kruit and J. P. Hoogenboom, *Struct. Dyn.*, 2019, **6**, 024102.
44 W. Verhoeven, J. F. M. van Rens, A. H. Kemper, E. H. Rietman, H. A. van Doorn, I. Koole, E. R. Kieft, P. H. A. Mutsaers and O. J. Luiten, *Rev. Sci. Instrum.*, 2019, **90**, 083703.
45 J. W. Lau, K. B. Schliep, M. B. Katz, V. J. Gokhale, J. J. Gorman, C. Jing, A. Liu, Y. Zhao, E. Montgomery, H. Choe, W. Rush, A. Kanareykin, X. Fu and Y. Zhu, *Rev. Sci. Instrum.*, 2020, **91**, 021301.
46 X. W. Fu, E. D. Wang, Y. B. Zhao, A. Liu, E. Montgomery, V. J. Gokhale, J. J. Gorman, C. G. Jing, J. W. Lau and Y. M. Zhu, *Sci. Adv.*, 2020, **6**, eabc3456.
47 C. J. R. Duncan, D. A. Muller and J. M. Maxson, *Phys. Rev. Appl.*, 2020, **14**, 014060.
48 M. R. Armstrong, K. Boyden, N. D. Browning, G. H. Campbell, J. D. Colvin, W. J. DeHope, A. M. Frank, D. J. Gibson, F. Hartemann, J. S. Kim, W. E. King, T. B. LaGrange, B. J. Pyke, B. W. Reed, R. M. Shuttlesworth, B. C. Stuart and B. R. Torralva, *Ultramicroscopy*, 2007, **107**, 356–367.
49 A. Gahlmann, S. Tae Park and A. H. Zewail, *Phys. Chem. Chem. Phys.*, 2008, **10**, 2894–2909.
50 Z. Tao, H. Zhang, P. M. Duxbury, M. Berz and C.-Y. Ruan, *J. Appl. Phys.*, 2012, **111**, 044316.
51 A. Gliserin, A. Apolonski, F. Krausz and P. Baum, *New J. Phys.*, 2012, **14**, 073055.
52 P. Baum and A. H. Zewail, *Proc. Natl. Acad. Sci. U. S. A.*, 2007, **104**, 18409–18414.
53 B. Barwick, H. S. Park, O. H. Kwon, J. S. Baskin and A. H. Zewail, *Science*, 2008, **322**, 1227–1231.
54 K. Bikker, M. Picher, O. Cregut, T. LaGrange, B. W. Reed, S. T. Park, D. J. Masiel and F. Banhart, *Ultramicroscopy*, 2016, **171**, 8–18.
55 E. Kieft, K. B. Schliep, P. K. Suri and D. J. Flannigan, *Struct. Dyn.*, 2015, **2**, 051101.
56 H. S. Park, J. S. Baskin, O. H. Kwon and A. H. Zewail, *Nano Lett.*, 2007, **7**, 2545–2551.
57 P. Baum, *Chem. Phys.*, 2013, **423**, 55–61.

58 D. A. Plemmons and D. J. Flannigan, *Chem. Phys. Lett.*, 2017, **683**, 186–192.
59 M. Aidelsburger, F. O. Kirchner, F. Krausz and P. Baum, *Proc. Natl. Acad. Sci. U. S. A.*, 2010, **107**, 19714–19719.
60 L. Piazza, D. J. Masiel, T. LaGrange, B. W. Reed, B. Barwick and F. Carbone, *Chem. Phys.*, 2013, **423**, 79–84.
61 S. A. Aseyev, A. S. Sadkov, B. N. Mironov, A. A. Ischenko, S. V. Chekalin and E. A. Ryabov, *J. Exp. Theor. Phys.*, 2019, **128**, 379–383.
62 K. Halbach and R. F. Holsinger, *Part. Accel.*, 1976, **7**, 213–222.
63 M. J. de Loos and S. B. van der Geer, *Proc. 5th Eur. Part. Acc. Conf., Sitges*, 1996, 1241.
64 Z. T. Pei and C. N. Berglund, *Jpn. J. Appl. Phys., Part 2*, 2002, **41**, L52–L54.
65 C. Weninger and P. Baum, *Ultramicroscopy*, 2012, **113**, 145–151.
66 S. Mogren and R. Reifenberger, *Surf. Sci.*, 1987, **186**, 232–246.
67 P. Baum, *J. Phys. B: At., Mol. Opt. Phys.*, 2014, **47**, 124005.
68 D. Kreier, D. Sabonis and P. Baum, *J. Opt.*, 2014, **16**, 075201.
69 K. Torgasin, K. Morita, H. Zen, K. Masuda, T. Katsurayama, T. Murata, S. Suphakul, H. Yamashita, T. Nogi, T. Kii, K. Nagasaki and H. Ohgaki, *Phys. Rev. Accel. Beams*, 2017, **20**, 073401.